Journal of Materials Chemistry C

Revealing Al evaporation-assisted functions in solution-processed ZnO thin film transistors

Journal:	*Journal of Materials Chemistry C*
Manuscript ID:	TC-ART-09-2014-002096.R1
Article Type:	Paper
Date Submitted by the Author:	10-Oct-2014
Complete List of Authors:	Kang, Taesung; Hanyang university, Physics Kim, Taeyoon; Hanyang university, Physics Yoon, Kapsoo; Samsung Display, IT development Kim, Jongmin; Dongguk university, Semiconductor Science Im, Hyunsik; Dongguk university, Semiconductor Science Jin Pyo, Hong; Hanyang University, Department of Physics

SCHOLARONE™
Manuscripts

Journal of Materials Chemistry C

Journal of Materials Chemistry C

Dynamic Article Links ►

Cite this: DOI: 10.1039/c0xx00000x

www.rsc.org/xxxxxx

Paper

Revealing Al evaporation-assisted functions in solution-processed ZnO thin film transistors

Tae Sung Kang[a], Tae Yoon Kim[a], Kap Soo Yoon[b], Jong Min Kim[c], Hyun Sik Im[c], and Jin Pyo Hong*[a]

Received (in XXX, XXX) Xth XXXXXXXXX 20XX, Accepted Xth XXXXXXXXX 20XX
DOI: 10.1039/b000000x

Metal oxide semiconductors based on a solution process have facilitated major breakthroughs in the emerging field of flexible and transparent electronic devices. In particular, enhanced output performance of metal oxide semiconductors obtained by a solution process is desirable, because they are easy to fabricate and cost effective at low temperatures. To date, a carbon-free method involving an aqueous zinc amine complex has been employed to generate metal oxide active layers that have outstanding electrical features despite formation of a very thin active layer. However, manipulation of trap states induced by chronic weak bonding structures initially present during the solution process remains a challenge. In addition, a thin active layer is highly susceptible to initial surface and interface charge traps, resulting in deterioration of electron transport by unclear mechanisms. Therefore, intentional control of intrinsic defects arising from porosity and pinholes is becoming one of the key issues in the development of highly stable solution-processed metal oxide semiconductors. Here, we describe a generic metal evaporation approach to enhance the electrical performance of solution-processed ZnO TFTs. In particular, we do not use passivation or post-annealing processes. Based on systematic structural and electrical analyses, we propose a mechanism based on Al metal evaporation-driven reduction of trap states that convincingly explains the unique features of the solution-processed ZnO TFTs obtained in this study. We anticipate that these findings will spur progress toward the realization of solution-processed electronic devices.

1. Introduction

Development of metal oxide semiconductors containing oxide materials such as Zn, Sn, In, Mg, and Ga is of great interest for numerous electronic and optoelectronic device applications.[1, 2] Among the materials considered recently, amorphous In-Ga-ZnO (IGZO) is a highly promising candidate as the main active media in thin film transistors (TFTs) in order to meet the demands of switching devices in next-generation displays, such as smart windows and transparent electric signboards. IGZO has highly distinct electron mobility (> 10 $cm^2 V^{-1}s^{-1}$) due to large metal s-orbitals that are relatively insensitive to bond angle disorder and an isotropic shape, compared to covalent semiconductors such as amorphous silicon.[3] In addition, IGZO has high electron mobility with a wide optical bandgap (3.3~3.5eV) even at low temperatures, enabling the use of IGZO TFTs in flexible and transparent window displays.[4] However, the widespread use of IGZO in TFTs is limited by the scarcity of indium and gallium. As such, much effort has been dedicated toward the achievement of indium-free metal oxide semiconductors via doping with various dopants such as Li, Na, Y or Sn in order to develop Zn-based metal oxide semiconductors.[5, 6] In particular, solution methods are simple, cost-effective, large-scale fabrication processes that can be performed at low temperatures and allow easy control of various dopants for the development of various metal-doped ZnO TFTs. Carbon-free solution-processed metal oxide films exhibit outstanding electrical performance at low temperatures (<300°C) because no carbon-based organic residuals are produced, such as acetate functional groups that are associated with residual problems arising from incomplete reactions of the ZnO films even at high temperatures (400°C).[7, 8] Therefore, the absence of organic impurities during growth of carbon-free metal oxide TFTs based on zinc amine complexes has been investigated.[9, 10] However, serious hurdles remain in the improvement of output performance, which is negatively impacted by the thinness (< 10 nm) of the active layer; a thin active layer is an inherent characteristic of growth at low temperatures due to high volatility, rapid decomposition, and concentration limitations.[11, 12] It is widely believed that a thin active layer limits the electrical performance and stability of solution-processed metal oxide semiconductors. Previous studies reported that thin active layers close to the field-induced electron transport region (~3 nm) provided spatial charge traps at the interface and surface, critically affecting electrical characteristics by creating a space charge region within the active layer.[13, 14] Continuously repeated spin-coating procedures might solve this issue, but intrinsic oxygen-related trap states arising from porosity and pinhole creation remain a challenge.[15] In addition, the solution process is highly susceptible to vulnerable

bonding between metal and oxygen in an air atmosphere.[16] A passivation approach that involves the incorporation of SiO_2, HfO_2, MgO, TiO_x, or Al_2O_3 materials has been used to reduce the effects of the environment on metal oxide TFTs.[17-19] However, the use of a passivation layer results in degradation of electrical features due to additional defects at the channel/passivation interface.[20] Recently, Zan et al. announced an innovative concept involving the use of nanometer dot doping and metal capping-processed metal oxide TFTs with high carrier mobility and stable device performance.[21, 22] However, these processes, which are based on sputtering of the IGZO active layer, may also physically damage the surface or promote chemical reactions on the surface during deposition. These processes might therefore not be appropriate for solution-processed ZnO TFTs that are intrinsically porous and have weak bonding structures. To suppress inherent state defects of solution-processed ZnO TFTs without the use of passivation layer, we introduced the concept of Al nanoparticle evaporation to obtain highly stable electrical features in an air atmosphere.[23] However, we did not address several key issues affecting electrical output and did not perform detailed structural/electrical analyses of the role of Al evaporation. In particular, we did not identify a convincing mechanism in our previous work.

In this letter, we examine the effect of simple Al evaporation on solution-processed ZnO TFTs through systematic structural/electrical measurements. Al evaporation times of 0 to 40 sec resulted in Al-evaporated ZnO TFTs with enhanced electrical features. A maximum carrier mobility of 35.27 cm^2 V^{-1} s^{-1} was obtained for 40-sec Al-evaporated ZnO TFTs, which is 18-fold higher than that of pristine ZnO TFTs (1.95 cm^2 V^{-1} s^{-1}). Optimized 20-sec Al-evaporated ZnO TFTs also exhibited an improved carrier mobility of 8.15 cm^2 V^{-1} s^{-1}, together with highly promising stability. We propose possible origins of solution-processed ZnO TFTs containing a ZnO active layer thinner than 10 nm based on oxygen-related deep level traps and metal bonding-related shallow traps. Finally, we conduct low temperature-dependent activation energy analyses under high vacuum conditions (~10^{-6} Torr), along with positive temperature bias stress (PBTS) tests at 70°C in an air atmosphere. More detailed descriptions of the process used to fabricate Al-evaporated ZnO TFTs are provided in the Experimental section.

2. Experimental

2.1 Preparation of ZnO film

ZnO solution was prepared by dissolving 0.005 moles of zinc oxide (Sigma Aldrich 99.999%) in 6 mL of ammonium hydroxide (aq) (Alfa Aesar, 99.9%). To increase the solubility of the ammonia water, the precursor solution of ZnO was kept in a refrigerator for 10 hours. After dissolution of the precipitated ZnO particles, the ZnO solution was deposited onto heavily B-doped n-type Si with thermally grown SiO_2 substrate (200 nm, C_{OX}= 17.25 nF cm^{-2}) by spin-coating for 60 sec at 5000 rpm to achieve a thickness of 7-8 nm, followed by annealing at 300°C for 1 hour. Before the deposition process, SiO_2 was serially cleaned with acetone, isopropyl alcohol, and deionized water.

2.2 Fabrication of Al-evaporated ZnO TFTs

The Al pellet was thermally evaporated under high vacuum (10^{-7} Torr) onto ZnO films at an Al deposition rate of 0.1Å s^{-1}. As soon as the Al evaporated, a UVC (wave length: 100-280 nm) irradiation process (to promote immaculate oxidation of Al) was performed for 5 min, followed by thermal annealing at 100°C for 15 min. Finally, 100-nm-thick Al electrodes were deposited on the ZnO film via thermal evaporation through a shadow mask. The channel length (L) was 50 μm, and the channel width (W) was 500 μm.

2.3 Electrical Characterization

Transistor current-voltage characteristics were measured under air and high vacuum (~10^{-6}) conditions using a Keithley 4200-Semiconductor Characterization System (4200-scs). Forward and reverse gate biases of hysteresis were analyzed between -20 and 40 V (at V_{DS} = 10V) in order to determine typical transfer curves. In addition, a positive bias temperature stability (PBTS) test was performed at 70°C for 3600 s in an air atmosphere (V_{GS}=20 V). Field-effect mobility and threshold voltage were derived by extracting the slope above the threshold voltage regime from the square root of the I_D vs. V_{GS} plot and the axis intercept, respectively. Activation energy was extracted from the transfer characteristics in the temperature range of 20-300 K under high vacuum (~10^{-6}). In addition, the carrier concentration, Hall mobility, and resistivity of films were confirmed by a Hall-effect measurement system (Lake Shore, model7662) using the van der Pauw method.

2.4 Structural & optical analysis

Film microstructures and depth profiles were investigated using high-resolution transmission electron microscopy (HRTEM) and energy dispersive X-ray spectroscopy (EDS) (JEOL, JEM-4010). Auger electron spectroscopy (AES, ULVAC, PHI 680) was also used to investigate the stoichiometry of Al-evaporated ZnO. For the optical bandgap, the transmittance of Al-evaporated ZnO films was measured using a UV-visible spectrometer (Lambda 35: PerkinElmer).

3. Results and discussion

3.1 Electrical and structural characteristics of ZnO TFTs under Al evaporation

Fig. 1a shows the transfer and hysteresis behaviors of Al-evaporated ZnO TFTs for Al evaporation times ranging from 0 sec to 40 sec. For convenience, as-grown, 10-sec, 20-sec, 30-sec, and 40-sec Al-evaporation ZnO TFTs were termed Samples A, B, C, D, and E, respectively. Drain-source current (I_{DS}), including enhanced hysteresis features, increased with longer Al evaporation time. It is widely believed that the hysteresis window feature is related to deep level trapped electrons with long release times, whereas field-effect mobility (μ_{FE}) is dominantly attributable to shallow donor trap states with short release times.[24] Sample A had the lowest μ_{FE} (1.95 cm^2 V^{-1} s^{-1}) and a large hysteresis feature, while Sample C exhibited a dramatically improved μ_{FE} (8.15 cm^2 V^{-1} s^{-1}) without hysteresis degradation. Furthermore, the latter device had highly improved μ_{FE} at annealing temperatures ranging from 100 to 300°C (see Fig. S1 in the ESI†). Improvement in both hysteresis and mobility after optimized Al evaporation reflects enhanced electron transport through the ZnO active layer. However, the longer evaporation time (40-sec) of Sample E led to an increase in off-current, despite an increase in the μ_{FE} to 35.27 cm^2 V^{-1} s^{-1}. The on/off ratio of Al-evaporated ZnO TFTs remained at ~10^{-7} for short Al evaporation times (0-20 sec) and then deteriorated significantly from ~10^{-7} to ~10^{-5} for longer Al

evaporation times (30-40 sec) (Fig. 1a). Therefore, longer Al evaporation times (>20 sec) may create metallic conduction paths on the ZnO surface, resulting in an increase in the off-current level.

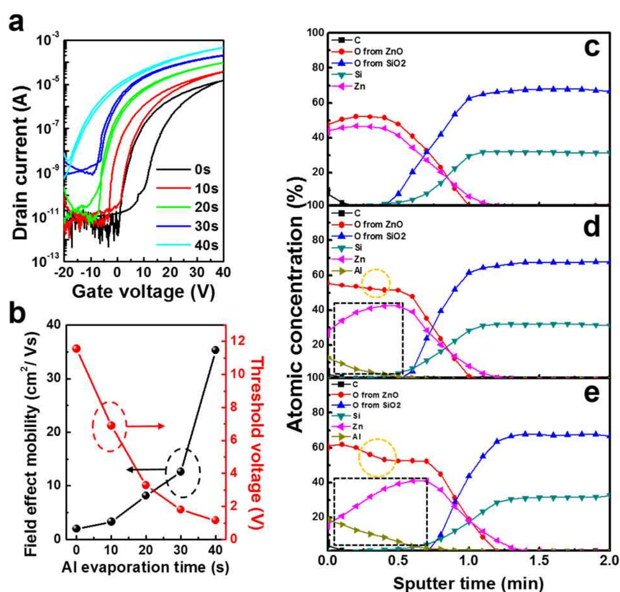

Fig. 1. Effect of Al evaporation time on the characteristics of solution-processed ZnO TFTs. (a) Transfer hysteresis loops of pristine ZnO (black line) and Al-evaporated ZnO TFTs, in which Al evaporation time was varied from 0 to 40 sec. Stable hysteresis behavior and enhanced electron transport with a high on/off ratio were observed for an Al evaporation time of 20 sec (green line). (b) Field-effect mobility (left axis) and threshold voltage (right axis) dependence of ZnO TFTs at different Al evaporation times. Auger electron spectroscopy (AES) depth profiles of (c) pristine ZnO, (d) 10-sec Al-evaporated ZnO, and (e) 20-sec Al-evaporated ZnO films showing the Al deposition time-dependent diffusion of Al ions (dashed black box). Increasing Al deposition time resulted in diffusion of a large amount of Al ions into the ZnO active layer.

To further determine the electrical features affected by Al evaporation time, output curves for Al-evaporated ZnO TFTs were plotted and are shown in Fig. S2. Threshold voltages (V_{th}) shifted negatively from 11.54 to 1.59 V with an increase in Al evaporation time from 0 to 40 sec (Fig. 1b). Such a negative shift in V_{th} is likely due to an increase in carrier concentration, because carrier density in the channel active layer is related to threshold voltage.[25] Furthermore, it has been reported that mobility in metal oxide semiconductors relies on the carrier concentration, and carrier transport in polycrystalline structures is governed mainly by localized trap states between the band gap.[26] Therefore, the enhanced μ_{FE} values we obtained are likely due to both increased carrier concentration and decreased trap states. To determine the distribution of Zn, Al, and O elements within the ZnO layer upon Al evaporation in the range of 0 – 20 sec, auger electron spectroscopy (AES) depth profiling was conducted, and results are shown in Figs. 1c-e. All layers illustrated clear Al ion diffusion toward the ZnO layer, as marked by the dashed black boxes. In addition, longer Al evaporation times of 30 and 40 sec resulted in increased Al atom diffusion (see Fig. S3 in the ESI†). Profiles of Zn and O atoms for Sample A without carbon impurities are shown in Fig. 1c. Increasing the Al evaporation time from 10 to 20 sec resulted in increased diffusion of Al ions and a reduction of Zn ions within the ZnO layer, as shown in Figs. 1d and 1e, respectively. The amount of oxygen ions in the ZnO layer (depicted by yellow dashed circles) also increased, possibly representing the presence of oxidized Al phases within the ZnO layer, arising from Al ions that impregnated the layer through diffusion. We hypothesized that the reduction of Zn ions corresponded to Al substitution for Zn, leading to the formation of Al-O bonds. The above findings were consistent for all other samples. To further investigate the Al evaporation-driven structural features of the ZnO layer, we performed cross-sectional HRTEM and EDS analyses (See Figs. S4 and S5 in the ESI†).

3.2 Electrical and optical responses of ZnO films according to Al evaporation time

To further investigate the electrical characteristics of ZnO films according to Al evaporation time, Hall mobility and carrier concentration of ZnO layers were determined using Hall measurements. As shown in Fig. 2a, both Hall mobility and carrier concentration increased with increasing Al evaporation time.

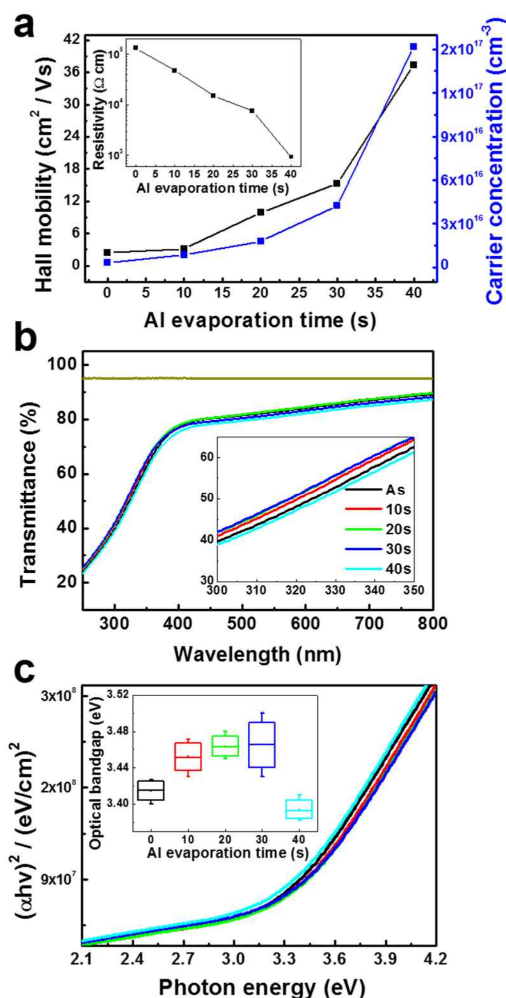

Fig. 2. Electrical and optical responses of solution-processed ZnO active layers recorded after Al evaporation. (a) Hall mobility and carrier concentration of pristine ZnO and Al-evaporated ZnO films, plotted as a function of Al evaporation time: the inset shows a plot of resistivity versus Al evaporation time. (b) Optical transmittance spectra of the pristine ZnO and Al-evaporated ZnO films grown on glass substrates: the inset reflects a slight variation in the transmittance depending on Al evaporation time. (c) Plots of $(\alpha h\nu)^2$ *vs.* photon energy for the pristine ZnO film and Al-evaporated ZnO films: the inset represents the variation in the optical band gaps upon Al evaporation, while the vertical error bars show the typical errors from the samples tested.

However, resistivity decreased with Al evaporation time, as shown in the inset of Fig. 2a. The carrier concentration of ZnO films for Al evaporation times ranging from 0 to 30 sec increased gradually from 3.1 x 10^{15} to 4.2 x 10^{16} and then increased up to 1.5 x 10^{17} at 40 sec. A similar pattern was observed for the Hall mobility according to Al evaporation time. Optical transmission spectra of ZnO layers grown on glass substrates as a function of Al evaporation time are shown in Fig. 2b. All layers had an average optical transparency greater than 80% in the visible wavelength range. The inset in Fig. 1b shows a gradual blue shift in the transmittance with an increase in Al evaporation times from 0 to 30 sec, while a red shift was observed for an Al evaporation time of 40 sec. Fig. 2c shows a plot of $(\alpha h\nu)^2$ versus photon energy for Al-evaporated ZnO layers, which was used to estimate the optical band gaps using the following Tauc relation:

$$(\alpha h\nu)^m = A(h\nu - E_{opt}) \qquad (1)$$

where α is the absorption coefficient (α= -1/d ln(1/T), d is the thickness of ZnO, T is the transmittance, and hν is the photon energy. m was experimentally found to be 2 for the direct model, and E_{opt} was calculated by extrapolating the linear region to the photon energy axis, as shown in the inset of Fig. 2c.[27] E_{opt} increased for Al evaporation times up to 30 sec and then decreased at 40 sec. The increase in E_{opt} can be interpreted based on Burstein-Moss effects: When the conduction band becomes significantly filled at a high doping concentration and the lowest energy states in the conduction band are blocked, E_{opt} increases in n-type semiconductors, and a parabolic band is produced according to the following equation:

$$\Delta E^{BM} = \frac{h^2}{8\pi^2 m^*}(3\pi^2 n)^{\frac{2}{3}} \qquad (2)$$

where ΔE^{BM} is the shift in the optical bandgap, h is Plank's constant, n is the carrier concentration, and m^* is the electron effective mass in the conduction band.[28] Equation (2) has proven effective in electronic transport modeling of many oxide materials over a wide range of doping levels.[29] The increase in the absorption edge of the optimized Al-evaporated ZnO layers indicated an increase in donor electrons, giving rise to higher Hall mobility.[30] The decreased E_{opt} for the longer Al evaporation time of 40 sec may have been caused by the presence of segregated Al atoms or the formation of Al metallic phases that were not fully oxidized. In this situation, a localized surface plasmon resonance effect may have occurred, because excess Al metal atoms suffered from a lack of natural oxidation or scattered and absorbed light, reducing the concentration of photo-induced carriers within the ZnO active layer.[31] The above relation between optical bandgap and carrier concentration may explain the increased off-current level of Al-evaporated ZnO TFTs versus pristine ZnO TFT, as shown in Fig. 1a. A detailed summary of the electrical characteristics and bandgap is provided in Table 1.

3.3 Physical models of electrical characteristics of pristine and Al-evaporated ZnO TFTs

Based on the above observations, we propose a physical model to explain the electrical behaviors of pristine and Al-evaporated ZnO TFTs, as illustrated in Fig. 3. The as-grown ZnO surface is highly susceptible to weakly bonded oxygen atoms and pore trap sites initially included during solution-processed growth. Thus, the active layer surface strongly attracts O^{2-} ions, resulting in development of a positive polar surface. This phenomenon permits free carriers present in the conduction band to be captured by O^{2} ions absorbed on the surface. Therefore, a depletion layer of electron trap states is created beneath the oxide surface, followed by a decrease in free carriers, as shown in Fig. 3a. Furthermore, electron transport in the less-than-10-nm-thick layer is dominantly affected by a space charge region arising from surface states rather than carrier scattering.[13] Thus, the appearance of a surface space charge region also has to be considered. Trapped charges in thin layers interact with field-induced charge carriers at the semiconductor-insulator interface through Coulombic forces,

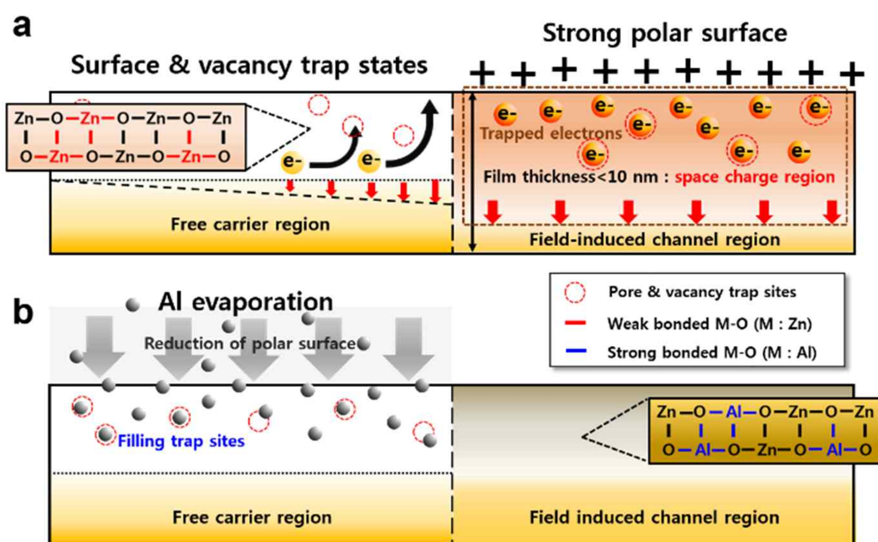

Fig. 3. Schematic illustration of charged surface trap states of pristine ZnO and Al-evaporated ZnO TFTs. (a) Schematic of pristine ZnO TFTs with an active layer < 10 nm thick, indicating the presence of strong polar surfaces functioning as electron trap sites (top left) and the appearance of a space charge region (top right). (b) Schematic of ZnO TFTs after evaporation of Al on the back channel surface, reflecting a reduction in the polar surface by replacement of initially formed weak M(Zn)-O bonds with strong M(Al)-O bonds formed after Al evaporation.

Table 1 Hall mobility, field-effect mobility, carrier concentration, and optical bandgap of pristine and Al-evaporated ZnO films as a function of various Al evaporation time.

Al evaporation time [sec]	Hall mobility [$Cm^2 V^{-1}s^{-1}$]	Field effect mobility [$Cm^2 V^{-1}s^{-1}$]	Carrier concentration [Cm^{-3}]	Optical band gap [eV]
Pristine ZnO	2.41	1.98	$3.115\cdot10^{15}$	3.414
10 sec	3.15	3.29	$8.467\cdot10^{15}$	3.451
20 sec	9.93	8.15	$1.788\cdot10^{16}$	3.462
30 sec	15.33	12.59	$4.224\cdot10^{16}$	3.469
40 sec	37.37	35.27	$1.517\cdot10^{17}$	3.392

leading to repulsion and trapping of free carriers within the channel region. As a result, a large number of electrically inactive paths form easily in the active layer of thin film semiconductors, which limits charge transport, resulting in an increase in threshold voltage. However, optimized Al evaporation on the ZnO layer permits thermally activated Al atoms from the back channel surface to impregnate the ZnO layer, as shown in Fig. 3b. Theoretical calculations imply Al atomic diffusion toward crystalline solids via a vacancy mechanism, because the formation energy of vacancies in n-type ZnO is relatively weak.[32] Impregnated Al atoms inside the ZnO layer form Al–O bonds with oxygen ions, because Al atoms have a greater reduction potential than Zn atoms.[33] This Al-O bonding may reduce the concentration of weakly bonded oxygen as well as defect states, significantly reducing the polar ZnO surface. Therefore, the number of electrically active paths increases and carrier mobility is enhanced. This model can explain the enhanced electrical behaviors obtained by optimizing Al evaporation time. Figs. S6 and S7 show the transfer characteristics of pristine, Al-evaporated, double-layered, and Al_2O_3 insulating layer-capped ZnO TFTs, which were determined to examine the possible roles of defect states in different configurations.

3.4 Analyses of activation energy of Al-evaporated ZnO TFTs

To gain insight into the relations between electron transport behaviors and trap states, the gate voltage dependence of the activation energy (E_a) of Samples A, B, and C was analyzed; results are shown in Figs. 4a-c. A previous study reported that deep trap states, mainly induced by oxygen molecules adsorbed in an air atmosphere, have a crucial influence on the generation of higher activation energy.[34] Therefore, we measured the transfer characteristics of our devices under a high vacuum of 10^{-6} Torr at low temperatures ranging from 80 to 300 K in order to prevent additional temperature-related oxygen adsorption. To predict activation energies, the temperature-dependent drain current was extracted from the transfer characteristics using the following Arrhenius equation:

$$I_{DS}=I_{DS0}\cdot\exp(-E_a/K_BT) \qquad (3)$$

where I_{DS0} is the prefactor of drain current, E_a is the activation energy, K_B is the Boltzmann constant, and T is the temperature (see Fig. S8 in the ESI†). Activation energies of all samples decreased with increasing gate voltage. This suggests a shift in the Fermi level (E_F) toward the conduction band edge (E_C) with increasing V_{GS}. In the sub-threshold regime (grey color) in Fig. 4a, Sample A had the maximum activation energy of 13 meV (the intersection of the top black dashed line at the y-axis), while Samples B and C had maximum activation energies of 16.7 meV and 19.3 meV,

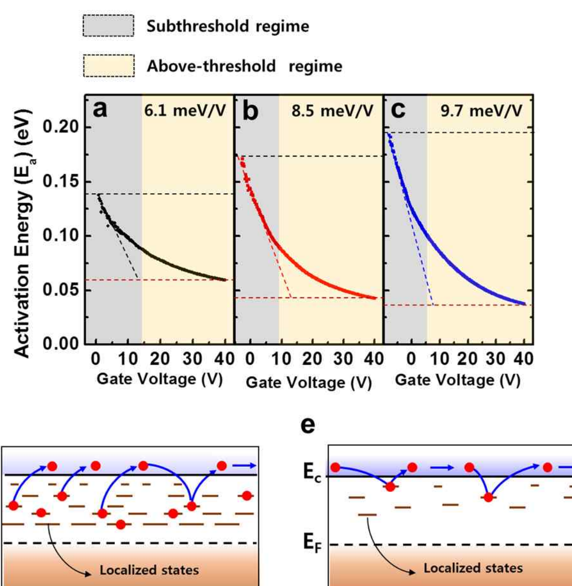

Fig. 4. Gate voltage dependence of activation energy (E_a) for (a) pristine [Sample A], (b) 10-sec Al-evaporated [Sample B], and (c) 20-sec Al-evaporated ZnO TFTs [Sample C]. Schematic depicting carrier transport origins for (d) pristine and (e) Al-evaporated ZnO TFTs, where the Fermi level (E_F) resides within the tail states. Orange dotted lines represent enlarged views of possible high and low traps sites occurring in the pristine and Al-evaporated active layers. Two different regimes are recognized: a sub-threshold regime (gray color) corresponding to a dominant trap charge density for electron transport, and an above threshold regime (yellow color), representing a transition from trap charge density to free carrier density nature near a conduction band edge.

respectively. We attributed the increase in activation energy of Samples B and C to reduction of trapped carriers positioned in localized trap states (Figs. 4b and c). The transfer characteristics of Sample A implies that the Fermi level (E_F) resides within localized trap states ($E_F \ll E_C$). Thus, when a large number of carriers are trapped in the localized trap states, the change in the drain current is negligible with decreasing temperature. This corresponds to a low activation energy, because trapped carriers are primarily governed by multiple trapping and releasing events, as depicted in Figs. 4d and 4e.[35] The higher activation energies of Samples B and C are due to replacement of weak Zn-O bonding with strong Al-O bonding, allowing for a reduction in oxygen-related trap states. Differences in activation energy may also be identified by the variation in falling rate ($|\Delta E_a/\ \Delta V_{GS}|$), which is inversely proportional to large traps in the active layer. The falling rate increased gradually from 6.1 meV/V to 9.7 meV/V with increasing Al evaporation time up to 20 sec. This also refers to reduced trapped carriers in localized states. In contrast, in the above-

threshold regime (yellow color) at high voltage, the observed activation energies were reversed: Sample A had a larger activation energy of 5.92 meV than Samples B (4.25 meV) and C (3.74 meV), as shown by the intersection of the bottom red dashed line at the y-axis. Lower activation energies in this regime are likely due to free carrier conduction mechanisms within the field-induced channel region. That is, because the Fermi level lies near the conduction band edge (E_F<E_C) in the above-threshold regime, free carriers induced by accumulated electrons become more numerous than trapped carriers.[36] Thus, the larger number of free carriers in Al-evaporated ZnO TFTs percolate between potential barriers in non-localized states, lowering the activation energy. This result is consistent with the transfer curves shown in Fig. 1.

3.5 Investigation of the operational stability of the pristine and Al-evaporated ZnO TFTs

According to the Le Chatelier principle, positive gate bias affects field-induced oxygen adsorption on the back channel surface.[37] Therefore, we analyzed positive gate bias stress (PBS) features (see Fig. S9 in the ESI†) to clarify the reactivity arising from oxygen molecule-related deep level traps. Furthermore, to investigate temperature-related oxygen behaviors, time evolution

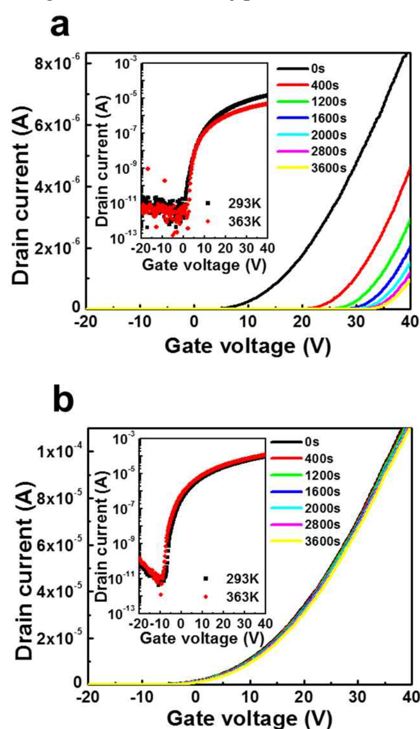

Fig. 5. Positive gate bias temperature stress-dependence of the electrical features of ZnO TFTs. Transfer traces of (a) pristine ZnO and (b) 20-sec Al-evaporated ZnO TFTs, measured at V_{GS}= 20 V and 70°C. Insets show the electrical characteristics of the samples recorded at the temperatures of 293 and 363 K, indicating the more stable features of the Al-evaporated sample than the pristine sample.

of representative transfer curves for Samples A and C under positive gate bias temperature stress (PBTS) was analyzed, as illustrated in Fig. 5. Bias stress on these TFTs was applied to a constant gate voltage of +20 V at 70°C in an air atmosphere for 3600 seconds. Sample A underwent a large positive threshold voltage shift of 18.44 V after PBTS for 3600 sec, while Sample C yielded a much smaller positive threshold voltage shift of 2.34 V under identical conditions (Figs. 5a and b). Note that Sample A had a degraded on-current in the above-threshold voltage region with increasing temperature from 293 to 363 K (inset of Fig. 5a). In contrast, Sample C displayed only a small negative shift without transfer degradation. This small shift was mainly due to the contribution from thermally activated carriers within the channel band-gap with increasing temperature (inset of Fig. 5b). Previously, Takata *et al.* reported that, in an air environment, stable adsorbed oxygen O_2^- ions are present on the ZnO surface below 100°C and capture electrons from the ZnO layer.[38] Therefore, thermally activated free carriers in Sample A suffered from electron scattering by repulsion of charged O_2^-, causing mobility to decrease with temperature elevation. In addition, bias stress induced a large positive threshold voltage shift due to oxygen ions or vacancies generated at the channel/dielectric interface, because solution-processed ZnO layers have intrinsic defects, such as pores and pinholes in the active layer, that lead to unavoidable weak Zn-O bonding despite the completeness of the chemical reactions. As a consequence, trap states result from loosely bound oxygen ions that move in the pristine ZnO layer when an electric field is applied. In contrast, the superior PBTS reliability of Sample C was due to efficient reduction of defect sites created by replacement of weak Zn-O bonding with strong Al-O bonding. Al-O bonding can protect the back channel surface against oxygen molecules under an ambient atmosphere. Observation of this phenomenon in Sample C confirms our previous assertion that stable electrical characteristics can be achieved if Al evaporation time is optimized.

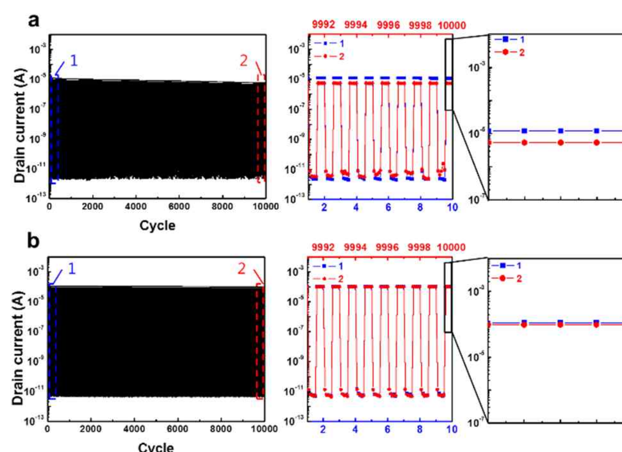

Fig. 6. Dynamic stress profiles of on- and off-states for 10,000 cycles. Stability behaviors of (a) pristine ZnO and (b) 20-sec Al-evaporated ZnO TFTs were measured at V_{gs}= 40 and – 10 V for the on and off states, respectively. The stress condition was a drain-source voltage of 10 V under 11 h stress duration in an air atmosphere. Right-most plots of (a) and (b) are enlarged views of selected regions 1 (blue dashed box) and 2 (red dashed box), respectively, showing the more stable output of Al-evaporated ZnO TFTs than pristine ZnO TFTs.

We also performed dynamic stress tests, in which Samples A and C were cycled continuously between on- (V_G = 40 V) and off-states (V_G = -10 V) in an air atmosphere, as shown in Fig. 6. The on-current level of Sample A deteriorated after 10^4 cycles of operation, with a 55% decrease in the rate of change and a decrease in the on/off ratio from 2.1×10^7 to 5.3×10^6. In contrast, Sample C remained unaffected by cycling, displaying only a 8.7% decrease in on-current and a stable on/off ratio of 1.8×10^7 after the same 10^4 continuous cycles of operation. Therefore, it is clear that an optimized Al evaporation process can increase the performance of solution-processed ZnO TFTs without the requirement for complicated passivation or doping processes.

4. Conclusions

In summary, we demonstrated that the device performance of solution-processed ZnO TFTs was affected by control of the carrier concentration and defect states via variation of the Al metal evaporation time. Optimization of the period of Al evaporation on the solution-processed ZnO TFTs resulted in an outstanding field-effect mobility of 8.15 $cm^2 V^{-1} s^{-1}$ without hysteresis degradation and an on/off current ratio of ~10^7. In addition to analyses of optical characteristics, structural observations using HRTEM, EDS, and AES, and UV-visible spectroscopy confirmed clear Al ion diffusion into the polycrystalline ZnO active layer. Enhancement in electrical features was predominantly due to reduction of weak Zn-O bonding related to shallow donor trap states through Al substitution of Zn and a decrease in adsorbed oxygen related to deep level trapping electrons through the passivation role of Al-evaporated ZnO TFTs. The mechanistic basis of the improvement in device output was determined by methodical analysis of low temperature measurements obtained under high vacuum (~10^{-7}) conditions. We anticipate that the ability to control and improve the electrical features of TFTs by optimizing Al metal evaporation time will lead to large-scale practical application of solution-processed oxide semiconductors.

Acknowledgements

This research was supported by a grant from the National Research Foundation of Korea (NRF) funded by the Ministry of Education (NRF-2013R1A1A2060350). Also, this work was supported by the Converging Research Center Program funded by the Ministry of Science, ICT & Future Planning (Project No. 2014048814).

Notes and references

[a] *Department of Physics, Hanyang University, Seoul, 133-791, South Korea, Fax :+82-2-2295-6868; Tel : +82-2-2220-0911; E-mail : jphong@hanyang.ac.kr*
[b] *Samsung Display IT Development, Cheonan-si,Chungcheongnam-do, South Korea.*
[c] *Department of Semiconductor Science, Dongguk University, Seoul 100-715, South Korea*
† Electronic supplementary information (ESI) available: The transfer characteristics of solution-processed ZnO TFTs evaporated by Al, the structural analyses of Al evaporated ZnO-TFTs with various deposition time, AES, TEM, EDS, and V_{th} shift under stress time data for ZnO thin films. See DOI: 10.1039/c000000x/

1 J. Elias, C. Levy-Clement, M. Bechelany, J. Michler, G. Y. Wang, Z. Wang, L. Philippe, *Adv. Mater.* **2010**, 22, 1607.
2 B. K. Sharma, B. Jang, J. E. Lee, S.-H. Bae, T. W. Kim, H.-J. Lee, J.-H. Kim, J.-H. Ahn, *Adv. Funct. Mater.* **2013**, 23, 2024.
3 K. Nomura, A. Takagi, T. Kamiya, H. Ohta, M. Hirano, H. Hosono, *Jpn. J. Appl. Phys.* **2006**, 45, 4303.
4 G. J. Lee, J. Kim, J.-H. Kim, S. M. Jeong, J. E. Jang, J. Jeong, *Semicond. Sci. Technol.* **2014**, 29, 035003.
5 S. Y. Park , B. J. Kim , K. Kim , M. S. Kang , K. H. Lim , T. Il Lee , J. M. Myoung , H. K. Baik , J. H. Cho , Y. S. Kim , *Adv. Mater.* **2012** , *24* , 834.
6 T. Jun, K. Song, Y. Jung, S. Jeong, J. Moon, *J. Mater. Chem.* **2011**, 21, 13524.
7 S. T. Meyers, J. T. Anderson, C. M. Hung, J. Thompson, J. F. Wager, D. A. Keszler, *J. Am. Chem. Soc.* **2008**, 130, 17603.
8 M. Ohyama, H. Kouzuka, T. Yoko, *Thin Solid Films* **1997**, 306, 78.
9 T. Jun, K. Song, Y. Jeong, K. Woo, D. Kim, C. Bae, J. Moon, *J. Mater. Chem.* **2011**, 21, 1102.
10 K. Kim, S. Y. Park, K.-H. Lim, C. Shin, J.-M. Myoung, Y. S. Kim, *J. Mater. Chem.* **2012**, 22, 23120.
11 S. Y. Park, S. Kim, J. Yoo, K.-H. Lim, E. Lee, K. Kim, J. Kim, Y. S. Kim, RSC Adv. **2014**, 4, 11295.
12 Y. H. Lin, H. Faber, K. Zhao, Q. Wang, A. Amassian, M. McLachlan, T. D. Anthopoulos, *Adv. Mater.* **2013**, 25, 4340.
13 L. Shao, K. Nomura, T. Kamiya, H. Hosono, *Electrochem. Solid-State Lett.* **2011**, 14, H197.
14 M. Ortel, S. Pittner, V. Wagner, *J. Appl. Phys.* **2013**, 113, 154502.
15 C. Bae, D. Kim, S. Moon, T. Choi, Y. Kim, B. S. Kim, J. S. Lee, H. Shin, J. Moon, *ACS Appl. Mater. Interfaces* **2010**, 2, 626.
16 T. S. Kang, J. H. Koo, T. Y. Kim, J. P. Hong, *Appl. Phys. Express* **2013**, 6, 011101.
17 D. Y. Yoo, E. Chong, D. H. Kim, B. K. Ju, S. Y. Lee, *Thin Solid Films* **2012**, 520, 3783.
18 H.-S. Seo, J.-U. Bae, D.-H. Kim, Y. Park, C.-D. Kim, I. B. Kang, I.-J. Chung, J.-H. Choi, J.-M. Myoung, *Electrochem. Solid-State Lett.* **2009**, 12, H348.
19 C. Sung-Hwan, H. Min-Koo, *IEEE Electron Devices Lett.* **2012**, 33, 396.
20 K. Nomura, T. Kamiya, H. Hosono, *Thin Solid Films* **2012**, 520, 3778.
21 H. W. Zan, W. W. Tsai, C. H. Chen, C. C. Tsai, *Adv. Mater.* **2011**, 23, 4237.
22 H. W. Zan, C. C. Yeh, H. F. Meng, C. C. Tsai, L. H. Chen, *Adv. Mater.* **2012**, 24, 3509.
23 T. S. Kang, T. Y. Kim, G. M. Lee, H. C. Sohn, J. P. Hong, *J. Mater. Chem. C* **2014**, 2, 1390.
24 K.-H. Lee, K.-C. Ok, H. Kim, J.-S. Park, *Ceramics International* **2014**, 40, 3215.
25 N. L. Dehuff, E. S. Kettenring, D. Hong, H. Q. Chiang, J. F. Wager, R. L. Hoffman, C. H. Park, D. A. Keszler, *J. Appl. Phys.* **2005**, 97, 064505.
26 E. Lee, J. Ko, K.-H. Lim, K. Kim, S. Y. Park, J. M. Myoung, Y. S. Kim, *Adv. Funct. Mater.* **2014**, 24, 4689.
27 A. Sarkar, S. Ghosh, S. Chaudhuri, A. K. Pal, *Thin Solid Films* **1991**, 204, 255.
28 B. Sernelius, K. F. Berggren, Z. C. Jin, I. Hamberg, C. Granqvist, *Phys. Rev. B* **1988**, 37, 10244.
29 I. Hamberg, C. Granqvist, K. Berggren, B. Sernelius, L. Engström, *Phys. Rev. B* **1984**, 30, 3240.
30 K. H. Lim, K. Kim, S. Kim, S. Y. Park, H. Kim, Y. S. Kim, *Adv. Mater.* **2013**, 25, 2994.
31 C. Langhammer, M. Schwind, B. Kasemo, I. Zorić, *Nano Lett.* **2008**, 8, 1461.
32 G.-Y. Huang, C.-Y. Wang, J.-T. Wang, *J. Appl. Phys.* **2009**, 105, 073504.
33 P. Vanysek, 'Electrochemical Series', in Handbook of Chemistry and Physics, ed. D. R. Lide, CRC Press, Boca Raton, FL, USA, 87th edn, **2006**.
34 W.-F. Chung, T.-C. Chang, H.-W. Li, S.-C. Chen, Y.-C. Chen, T.-Y. Tseng, Y.-H. Tai, *Appl. Phys. Lett.* **2011**, 98, 152109.
35 C.-J. Ku, Z. Duan, P. I. Reyes, Y. Lu, Y. Xu, C.-L. Hsueh, E. Garfunkel, *Appl. Phys. Lett.* **2011**, 98, 123511.
36 S. Lee, K. Ghaffarzadeh, A. Nathan, J. Robertson, S. Jeon, C. Kim, I. H. Song, U. I. Chung, *Appl. Phys. Lett.* **2011**, 98, 203508.
37 D. Kang, H. Lim, C. Kim, I. Song, J. Park, *Appl. Phys. Lett.* **2007**, 90, 192101.
38 M. Takata, D. Tsubone, H. Yanagida, *J. Am. Ceram. Soc.* **1976**, 59, 4.

We have added text and GA image.

Image :

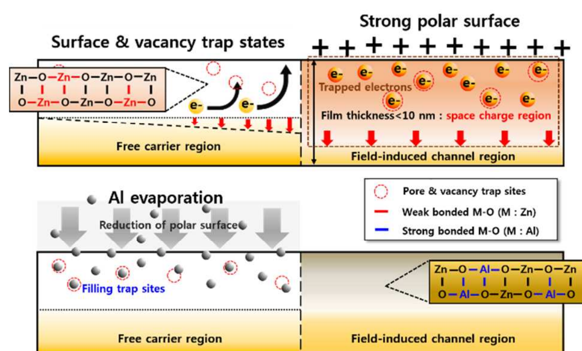

Text:

Impregnated Al atoms inside the ZnO layer form Al–O bonds with oxygen ions and may reduce the concentration of weakly bonded oxygen as well as space charge region, significantly reducing the polar ZnO surface.